

SINGLE JET INCLUSIVE PRODUCTION
FOR THE INDIVIDUAL JET p_T SCALE CHOICE
AT THE LHC*

JAMES CURRIE, E.W.N. GLOVER

Institute for Particle Physics Phenomenology, Department of Physics
University of Durham, Durham, DH1 3LE, UK

THOMAS GEHRMANN

Department of Physics, Universität Zürich
Winterthurerstrasse 190, 8057 Zürich, Switzerland

AUDE GEHRMANN-DE RIDDER, ALEXANDER HUSS

Institute for Theoretical Physics, ETH, 8093 Zürich, Switzerland

JOÃO PIRES

Max-Planck-Institut für Physik, Föhringer Ring 6, 80805 Munich, Germany

(Received April 4, 2017)

We study the single jet inclusive cross section up to next-to-next-to leading order in perturbative QCD, implemented in the parton-level event generator NNLOJET. Our results are fully differential in the jet transverse momentum and rapidity, and we apply fiducial cuts for comparison with the available ATLAS 7 TeV 4.5 fb^{-1} data for jet radius $R = 0.4$. For the theoretical calculation, we employ the antenna subtraction method to reliably cancel all infrared divergences present at intermediate stages of the calculation. We present all results using the individual jet transverse momentum $\mu_R = \mu_F \sim p_T$ as the renormalization and factorization scale for each jet's contribution to the single jet inclusive cross section. Finally, we consider the differences between our predictions using this scale choice to those for the leading jet transverse momentum scale choice, with reference to the ATLAS data.

DOI:10.5506/APhysPolB.48.955

* Presented at the Cracow Epiphany Conference “Particle Theory Meets the First Data from LHC Run 2”, Kraków, Poland, January 9–12, 2017.

1. Introduction

The single jet inclusive cross section is one of the most basic observables at any hadron collider. At its heart, there is the $2 \rightarrow 2$ QCD subprocess which already at leading order (LO) carries a dependence on the strong coupling, α_s , and significant sensitivity to the parameterization and value of the gluon's Parton Distribution Function (PDF), as can be seen in Fig. 1. It is clear that the gg and qg initial states dominate the production of jets over much of the experimentally accessible range in transverse momentum.

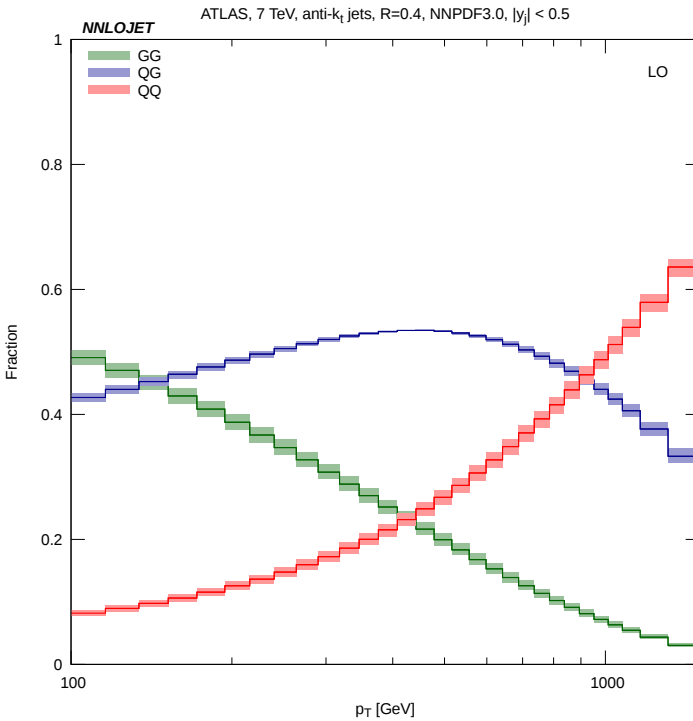


Fig. 1. (Colour on-line) The fraction of jets associated with a given initial-state for inclusive jet production calculated at LO for the LHC at 7 TeV. The different bands denote different initial-states: gg (grey/green), qg (dark grey/blue), qq (light grey/red). The relative size of the contributions goes from $gg > qg > qq$ at low p_T to an inverted hierarchy $qq > qg > gg$ at high p_T .

This observable has been measured by the ATLAS [1] and CMS [2] experiments at the LHC and has been used for determinations of α_s [3, 4] and in global PDF fits [5–7]. These studies have so far been carried out using theoretical predictions at next-to-leading order (NLO) accuracy in the strong coupling [8–10] which is typically accurate at the 10% level (although this

can be higher or lower in specific regions of phase space). Where jet data has been included in NNLO PDFs, this has been done using approximate NNLO predictions based upon threshold resummation techniques [11, 12].

The single jet inclusive cross section approximately scales with the jet transverse energy, E_T , as

$$\frac{d^2\sigma}{dp_T dy} \sim E_T^{-5}. \quad (1)$$

The dominant systematic error in the measurement of jets comes from the Jet Energy Scale (JES) [13] which is typically at the level of 1–2% for central jets at moderate p_T (but significantly larger for very high p_T and forward rapidity bins). This uncertainty in the jet energy translates into a systematic uncertainty on the cross section of ~ 5 –10%, as is confirmed by the detailed quantitative study of such errors in [1].

To improve the theoretical description of the single jet inclusive cross section in line with experimental advances, we have recently reported the calculation of the next-to-next-to leading order (NNLO) correction to jet production [14]. The inclusion of the NNLO contribution should systematically reduce the theoretical uncertainty as estimated by the magnitude of the variation of the observable upon variation of the unphysical renormalization, μ_R , and factorization, μ_F , scales.

2. Jets at the LHC

To make a connection between a parton-level calculation in perturbation theory and the experimentally observable jet found in the detector, it is necessary to employ a jet algorithm to cluster both the partons of the theoretical calculation and the energy deposits in the calorimeter into jets. The most commonly used class of jet algorithms for the LHC era jet studies are the sequential recombination algorithms. These algorithms are characterized by a resolution parameter, R , and an integer, p , [15]. The algorithm begins with the set of parton momenta coming from a point in phase space and sequentially clusters the momenta into “proto-jets” using the *distance* measures

$$\begin{aligned} d_{ij} &= \min\left(p_{T,i}^{2p}, p_{T,j}^{2p}\right) \frac{R_{ij}^2}{R^2}, & R_{ij}^2 &= (y_i - y_j)^2 + (\phi_i - \phi_j)^2, \\ d_{iB} &= p_{T,i}^{2p}. \end{aligned} \quad (2)$$

If the smallest distance calculated is a d_{ij} , then the two proto-jet momenta are merged using a “recombination scheme” into a single proto-jet and the algorithm starts over. The standard recombination scheme is the “4-vector”

scheme which simply adds the 4-momenta of the proto-jets and so generically produces massive proto-jets from massless partons. If the smallest distance calculated is a d_{iB} , then that proto-jet is removed from the list of proto-jets, stored as a “jet candidate” and the algorithm starts over. Once all proto-jets have been iteratively merged or removed and labelled as jet candidates, the algorithm terminates. We then apply the fiducial cuts to the set of jet candidates and those which survive the cuts are identified as jets which can be compared to data. Different choices of the parameter p define different algorithms with the k_T [16], Cambridge/Aachen [17] and anti- k_T [18] algorithms defined for $p = 1, 0$ and -1 respectively. The value of the resolution parameter R defines how far in y - ϕ space (which provides cylindrical coordinates for the detector geometry) the algorithm reaches out to merge proto-jets. For the purposes of comparing to ATLAS data, we employ the anti- k_T jet algorithm with $R = 0.4$ throughout this paper.

3. Antenna subtraction

It is well-known that the various contributions to the physical cross section, as calculated in perturbation theory, contain infrared (IR) singularities, either as explicit poles in the dimensional regularization parameter $\epsilon = (4 - d)/2$ or as unregulated divergences in the phase space integrals over parton-momenta.

For inclusive jet production at NNLO, we have the double real (RR) contribution given by the tree-level six-parton amplitude squared [19], the real-virtual (RV) contribution given by the interference of the one-loop with the tree-level five parton amplitudes [20–22], and the double virtual (VV) given by the interference of the two-loop with tree-level and self-interference of the one-loop four-parton amplitudes [23–25].

These contributions can be integrated numerically in four dimensions by introducing a set of local subtraction terms so as to reorganize the NNLO partonic cross section for initial-state partons of species i, j , into the form of

$$\begin{aligned}
 d\hat{\sigma}_{ij}^{\text{NNLO}} &= \int d\Phi_4 [d\hat{\sigma}_{ij}^{\text{RR}} - d\hat{\sigma}_{ij}^{\text{S}}] \\
 &+ \int d\Phi_3 [d\hat{\sigma}_{ij}^{\text{RV}} - d\hat{\sigma}_{ij}^{\text{T}}] \\
 &+ \int d\Phi_2 [d\hat{\sigma}_{ij}^{\text{VV}} - d\hat{\sigma}_{ij}^{\text{U}}] .
 \end{aligned} \tag{3}$$

The subtraction terms are constructed from antenna functions [26, 27] and reduced multiplicity matrix elements. The details of the construction of the various subtraction terms can be found in [26, 28].

4. Theoretical scale choice

The single jet inclusive cross section is accumulated by binning every jet in an event with at least one jet according to its transverse momentum, p_T , and rapidity, y . As such, it is important to remember that a single event can contribute several times to the distributions. For the theoretical calculation, each jet is binned with a weight which depends on the value of the appropriate PDF and α_s , which, in turn, depends on the chosen values of the theoretical scales μ_F and μ_R respectively. The fact that contributions to inclusive distributions come from individual jets rather than events introduces an ambiguity to the choice of theoretical scale; should we set the theoretical scales to reflect the hardness of the individual jets or the event from which they originated?

In a previous study [14], we set the theoretical scales equal to the transverse momentum of the hardest jet in the event, denoted p_{T_1} . This is an event-wide scale choice and is applied to the weights carried by *all* jets in an event, such that in a four-jet event, the value of α_s and the PDF weight is the same for the contribution of the fourth jet as it is for the leading jet.

An alternative is to use the individual jet p_T as the theoretical scale for each jet entering the distribution. For the leading jet in the event, this scale is identical to p_{T_1} and so 1-jet events, where only a single jet survives the fiducial cuts, are insensitive to the scale choice between p_T and p_{T_1} . Similarly, 2-jet events where the jets are balanced in p_T cannot generate any difference as $p_T = p_{T_1} = p_{T_2}$. Away from these jet configurations, the subleading jets will have smaller p_T than the leading jet in the event and so choosing the individual jet p_T as the theoretical scale will mean that the scale used to calculate the weight associated with a jet will on average be smaller than the scale p_{T_1} . A smaller value of μ_R will induce a larger value of α_s for the subleading jets and a smaller value of μ_F will alter the relative values of the PDFs. These differences will affect the calculated cross section in regions of phase space where the p_T of the subleading jets differs significantly from p_{T_1} , particularly for jets with low transverse momentum.

5. Results for $\mu_R, \mu_F \sim p_T$

The results presented here are for the experimental setup (p_T and rapidity bin widths) used by the ATLAS Collaboration for the $\sqrt{s} = 7$ TeV 4.5 fb^{-1} data set with jets reconstructed using the anti- k_T jet algorithm with $R = 0.4$. The cuts imposed on the jet data include all jets found with $p_T \geq 100$ GeV and $|y| < 3$. The theoretical calculation uses the NNPDF3.0 NNLO PDF set with $\alpha_s(M_Z^2) = 0.118$ for LO, NLO and NNLO contributions. The unphysical theoretical scales are set equal to the individual jet p_T such that for a jet with transverse momentum p_T , $\mu_R = \mu_F = p_T$ is the central scale choice. To obtain an estimate of the residual theoretical

uncertainty associated with the unphysical scales, we vary the central scale choice by factors of two and one half to obtain an envelope of predictions for the cross section.

In Fig. 2, we show the NLO/LO, NNLO/NLO and NNLO/LO K -factors across a range of p_T and rapidity bins. For the central rapidity bin, the NLO/LO K -factor is small and positive at low p_T and grows to $\sim 20\%$ at 1 TeV. In contrast, the NNLO/NLO K -factor provides a negative $\sim 10\%$ correction at low p_T and decreases in magnitude at higher p_T . The overall behaviour of the higher order corrections is encapsulated in the NNLO/LO K -factor which is driven by the NNLO correction at low p_T and the NLO correction at high p_T . As the rapidity of the jets increases, we see that the low p_T K -factors are similar to those of the central bin. At high p_T , the NLO/LO K -factor varies from a large positive correction in the central bin to a moderate negative correction in the most forward rapidity bin.

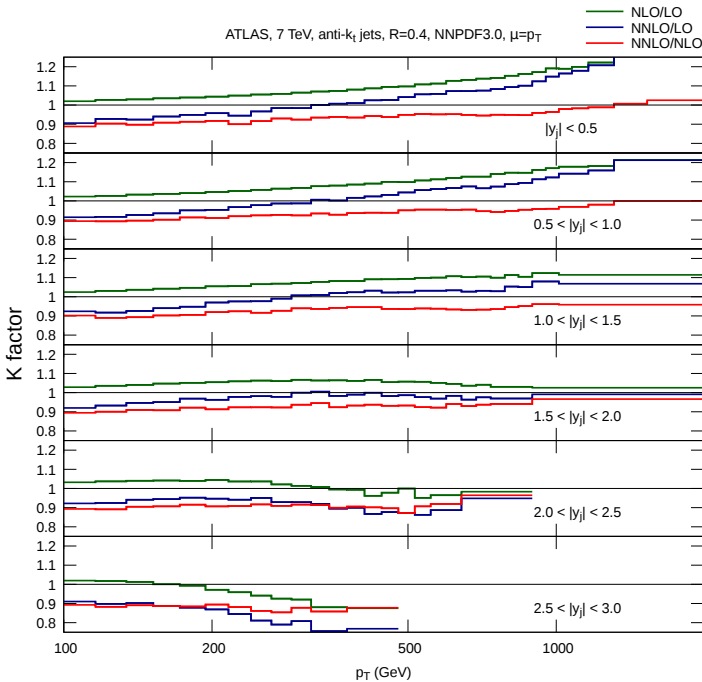


Fig. 2. (Colour on-line) NLO/LO (grey/green), NNLO/NLO (light grey/red) and NNLO/LO (black/blue) K -factors for jet production at $\sqrt{s} = 7$ TeV. The lines correspond to the double differential K -factors (ratios of perturbative predictions in the perturbative expansion) for $p_T > 100$ GeV and across six rapidity $|y|$ slices. Lines correspond to theoretical predictions evaluated with NNLO PDFs from NNPDF3.0 and central scale choice $\mu_R = \mu_F = p_T$.

In addition to the size and shape of the theoretical predictions, the NNLO contribution can affect the residual scale variation. In Fig. 3, we show how the cross section changes upon variation of the renormalization and factorization scales in a low, medium and high p_T bin for central rapidity. Across all bins, we observe that for fixed μ_F , the LO cross section varies monotonically with the variation of the renormalization scale, as is to be expected, as μ_R only affects the value of α_s at LO.

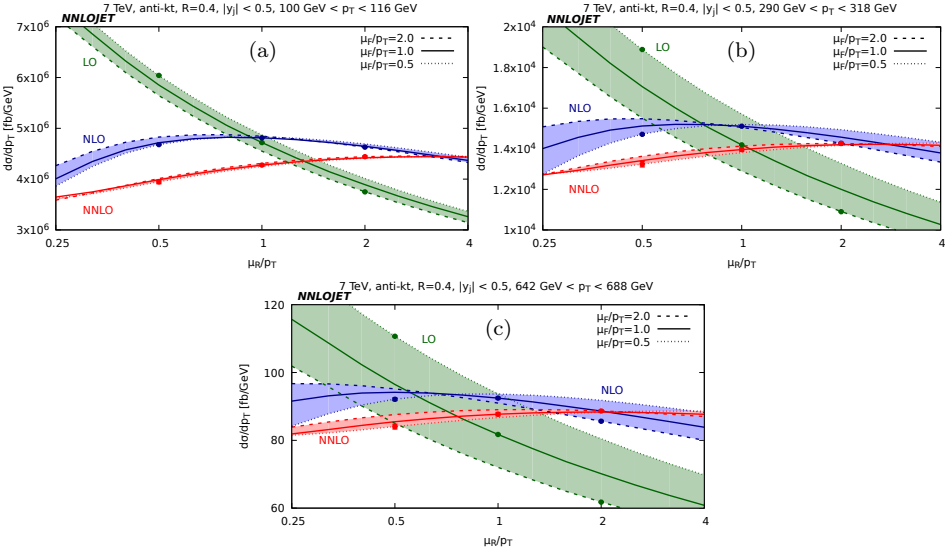


Fig. 3. (Colour on-line) The scale variation of the cross section at LO (grey/green), NLO (dark grey/blue) and NNLO (light grey/red) for central rapidity and three different p_T bins: (a) $100 \text{ GeV} < p_T < 116 \text{ GeV}$, (b) $290 \text{ GeV} < p_T < 318 \text{ GeV}$, (c) $642 \text{ GeV} < p_T < 688 \text{ GeV}$.

At NLO, we observe a more complicated variation due to the appearance of scale logarithms in the calculation which can oppose the variation coming from the strong coupling for $\mu_R, \mu_F < \mu_0$, where μ_0 is the central scale choice, *i.e.* p_T . The resultant shape has a maximum in the region of $\mu_R/p_T \sim 0.5$ – 1 depending on the p_T bin. The peaked shape of NLO curve ensures that the variation of the cross section due to μ_R is always negative compared to the central value. The position of the peak is close to the central scale choice, which means that the scale band is minimized when varying the scale about this value. Whilst such a band gives a true account for the range of values taken by the cross section upon variation, it gives a misleading estimate of the degree to which the cross section is changing in response to the scale variation.

At NNLO, we observe that the curve has less curvature than the NLO curve and is approximately linear with a decreasing gradient for increasing p_T . The variation of the NNLO cross section due to μ_R is larger than NLO in the low p_T bin, largely owing to the fact that the peaked shape of the NLO curve probably underestimates the uncertainty; but even taking this into account, the magnitude of the variation is similar to that at NLO. At higher p_T , the μ_R scale variation of the NNLO cross section decreases as the curve flattens in Fig. 3(c). At low p_T , the change due to μ_F variation, displayed as the thickness of the bands in Fig. 3, is relatively small, even at LO; whereas at high p_T , the μ_F variation becomes large at LO and is significantly reduced by including the NLO and especially NNLO corrections.

The information in Figs. 2 and 3 can be combined and compared to the available ATLAS data, as shown in Fig. 4. We observe that at low p_T , the NLO prediction shows some tension with the data, which lies approximately

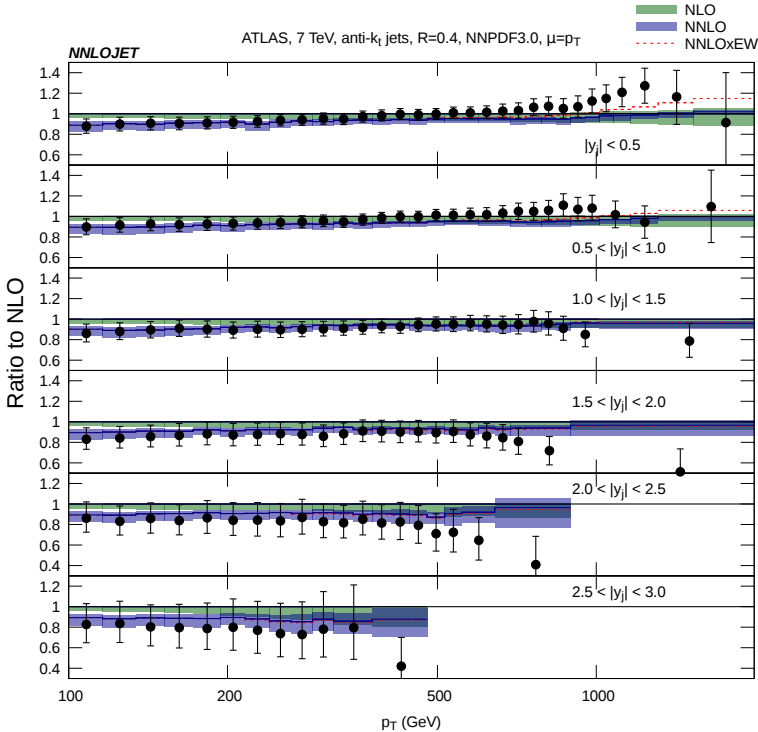


Fig. 4. (Colour on-line) The NLO (grey/green), NNLO (dark grey/blue) and ATLAS data normalized to the NLO prediction for the individual jet p_T scale choice. The bands correspond to the variation of $\mu = \mu_R = \mu_F$ by factors of 0.5 and 2 about the central scale choice. Electroweak correction are applied multiplicatively and separately represented as a dashed/red line.

10% below the NLO prediction. The NNLO correction acts negatively and brings the theoretical prediction in line with the data. At medium and high p_T , the theoretical prediction is largely consistent with the data and at very high p_T and central rapidity, the difference between the NNLO prediction and data can be largely accounted for by including the NLO electroweak corrections [29].

6. Comparison to $\mu_R, \mu_F \sim p_{T1}$

In addition to comparing to data, we can also compare to the same NNLO calculation, using the leading jet p_T as the theoretical scale, as reported in [14]. In Fig. 5, we show the NLO predictions for difference scale choices, normalized to the data. We see that at low p_T , there is a significant difference between the predictions for the different scale choices with the p_{T1} scale choice sitting close to the data, whereas the p_T scale choice lies approximately 10% above the data in the lowest p_T bin for central rapidity. The scale bands at low p_T are of similar size for the two scale choices.

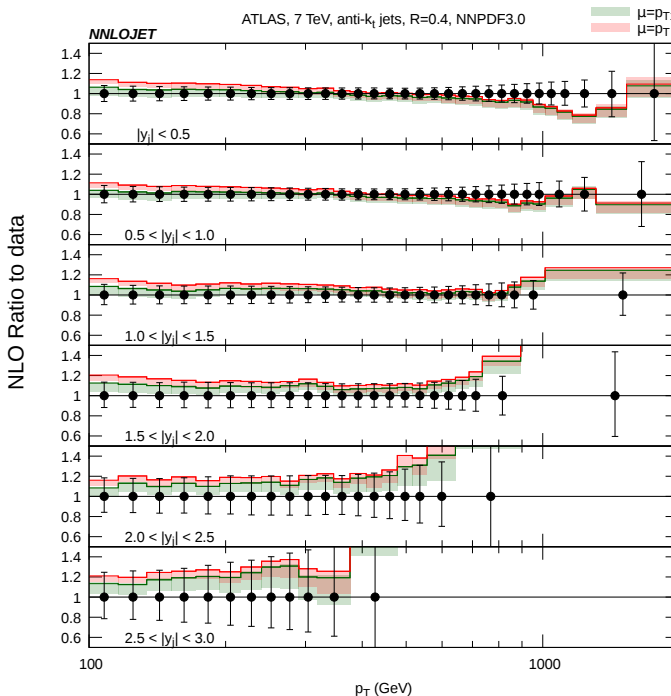


Fig. 5. (Colour on-line) The NLO predictions normalized to data for two different scale choices, individual jet p_T (grey/red) and leading jet p_T (dark grey/green). The bands correspond to the variation of $\mu = \mu_R = \mu_F$ by factors of 0.5 and 2 about the central scale choice.

At high p_T , we observe that the predictions for the two scale choices converge, particularly for central rapidities. The NLO scale bands are once again similar in size for the two scale choices and similar in size to the scale bands at low p_T .

In Fig. 6, we show the analogue of Fig. 5 at NNLO, again for the two scale choices. At low p_T , we find the behaviour somewhat different to NLO: the NNLO correction for the p_{T_1} scale moves the prediction away from the data, with which it was consistent at NLO; whereas using the p_T scale brings the NNLO prediction in line with the data with which there was some tension at NLO. The NNLO scale band is larger than the NLO scale band for both scale choices in the lowest p_T bin. At high p_T , the predictions for the two scale choices once again converge, as is to be expected for the largely back-to-back configurations found at high p_T . The NNLO scale band for the p_T scale choice offers only a moderate improvement over the NLO scale band in the p_T range of 300–900 GeV (and deterioration below this range), whereas the

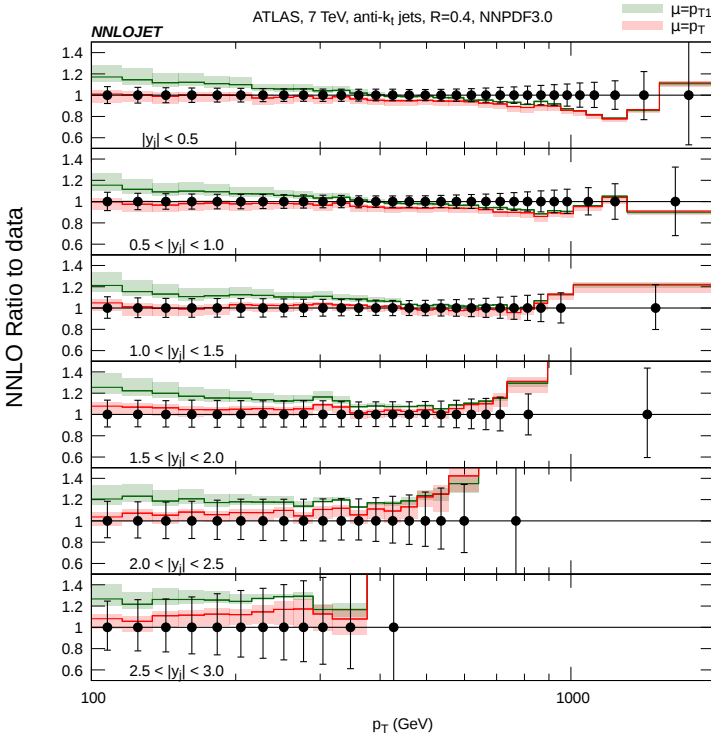


Fig. 6. (Colour on-line) The NNLO predictions normalized to data for two different scale choices, individual jet p_T (grey/red) and leading jet p_T (dark grey/green). The bands correspond to the variation of $\mu = \mu_R = \mu_F$ by factors of 0.5 and 2 about the central scale choice.

p_{T_1} scale choice shows a more dramatic reduction in scale uncertainty above 400 GeV and a more dramatic deterioration below 300 GeV. For p_T above 900 GeV, both scale choices show a similar reduction in scale uncertainty when passing from NLO to NNLO predictions.

7. Discussion

The individual jet p_T scale choice sets the scale dynamically for each jet in the distribution rather than at a scale reflecting the hardness of the event. This scale choice can only produce different results to the previously published results using the leading jet p_T scale choice when the subleading jets in an event have a p_T differing from the leading jet and this generically occurs for low p_T jets in the distributions considered here.

In the low p_T region, we find significant differences between the central values for the predictions using the two scale choices at NLO and NNLO. The uncertainty due to scale variation about those central scales also increases from NLO to NNLO for both scale choices and despite this increase, the bands do not overlap at low p_T . At higher p_T , the difference between the two scale choices decreases, as does the uncertainty due to scale variation, although the reduction in scale variation is more marked for the p_{T_1} scale for moderate p_T and central rapidities.

The comparison to ATLAS data, as shown in Figs. 5 and 6, exemplifies this difference in the scale choice. At NLO, we observe that the p_{T_1} scale choice sits closer to the data, whereas at NNLO, the fortunes are reversed and the p_T scale choice is more consistent¹. The inconsistencies between the theoretical calculations clearly poses a problem when it comes to deciding which scale should be used when comparing to data or fitting PDFs.

The NNLO calculation with p_T scale choice appears to provide a good description of the data, better than with the p_{T_1} scale choice. However, it achieves this by generating a relatively large NNLO/NLO K -factor alongside a slightly deteriorating scale dependence. As an unphysical scale in the theoretical calculation, there is no *a priori* preferred parameterization except for scales which minimize the disruptive influence of large logarithms on the perturbative expansion. It is often sensible to choose a scale which reflects the underlying Born-level kinematics, which for jet production is the LO $2 \rightarrow 2$ scattering where the two scales considered here coincide. The significant effect of this scale ambiguity on the NNLO predictions, and the lack of a theoretically well-motivated preference, motivates further study of this issue and consideration of non-standard scale choices to ensure the greatest possible phenomenological impact from jet data.

¹ The data is being used here merely as a reference point; we are using NNLO PDFs and so any genuine comparison of the NLO predictions to data is inappropriate. In any case, the NLO PDF has been fitted to this data for the scale choice p_T .

The authors thank Xuan Chen, Juan Cruz-Martinez, Tom Morgan and Jan Niehues for useful discussions and their many contributions to the NNLOJET code. We gratefully acknowledge the assistance provided by Jeppe Andersen utilizing the computing resources provided by the WLCG through the GridPP Collaboration. This research was supported in part by the UK Science and Technology Facilities Council, in part by the Swiss National Science Foundation (SNF) under contracts 200020-162487 and CRSII2-160814, in part by the Research Executive Agency (REA) of the European Union under the Grant Agreement PITN-GA-2012-316704 (“HiggsTools”) and the ERC Advanced Grant MC@NNLO (340983).

REFERENCES

- [1] G. Aad *et al.* [ATLAS Collaboration], *Eur. Phys. J. C* **71**, 1512 (2011); **73**, 2509 (2013); *J. High Energy Phys.* **1502**, 153 (2015) [*Erratum ibid.* **1509**, 141 (2015)].
- [2] V. Khachatryan *et al.* [CMS Collaboration], *Eur. Phys. J. C* **76**, 451 (2016); *J. High Energy Phys.* **1206**, 036 (2012); *Phys. Rev. Lett.* **107**, 132001 (2011).
- [3] B. Malaescu, P. Starovoitov, *Eur. Phys. J. C* **72**, 2041 (2012).
- [4] V. Khachatryan *et al.* [CMS Collaboration], *Eur. Phys. J. C* **75**, 288 (2015).
- [5] R.D. Ball *et al.* [NNPDF Collaboration], *J. High Energy Phys.* **1504**, 040 (2015).
- [6] L.A. Harland-Lang, A.D. Martin, P. Motylinski, R.S. Thorne, *Eur. Phys. J. C* **75**, 204 (2015).
- [7] S. Dulat *et al.*, *Phys. Rev. D* **93**, 033006 (2016).
- [8] Z. Nagy, *Phys. Rev. Lett.* **88**, 122003 (2002); *Phys. Rev. D* **68**, 094002 (2003).
- [9] S. Alioli *et al.*, *J. High Energy Phys.* **1104**, 081 (2011).
- [10] J. Gao *et al.*, *Comput. Phys. Commun.* **184**, 1626 (2013).
- [11] M.C. Kumar, S.O. Moch, *Phys. Lett. B* **730**, 122 (2014).
- [12] D. de Florian *et al.*, *Phys. Rev. Lett.* **112**, 082001 (2014).
- [13] G. Aad *et al.* [ATLAS Collaboration], *Eur. Phys. J. C* **75**, 17 (2015).
- [14] J. Currie, E.W.N. Glover, J. Pires, *Phys. Rev. Lett.* **118**, 072002 (2017).
- [15] G.P. Salam, *Eur. Phys. J. C* **67**, 637 (2010).
- [16] S.D. Ellis, D.E. Soper, *Phys. Rev. D* **48**, 3160 (1993).
- [17] M. Wobisch, T. Wengler, in: Hamburg 1998/1999, Monte Carlo Generators for HERA Physics, pp. 270–279 [[arXiv:hep-ph/9907280](https://arxiv.org/abs/hep-ph/9907280)].
- [18] M. Cacciari, G.P. Salam, G. Soyez, *J. High Energy Phys.* **0804**, 063 (2008).
- [19] M.L. Mangano, S.J. Parke, *Phys. Rep.* **200**, 301 (1991).
- [20] Z. Bern, L.J. Dixon, D.A. Kosower, *Phys. Rev. Lett.* **70**, 2677 (1993).

- [21] Z. Bern, L.J. Dixon, D.A. Kosower, *Nucl. Phys. B* **437**, 259 (1995).
- [22] Z. Kunszt, A. Signer, Z. Trocsanyi, *Phys. Lett. B* **336**, 529 (1994).
- [23] E.W.N. Glover, C. Oleari, M.E. Tejeda-Yeomans, *Nucl. Phys. B* **605**, 467 (2001); E.W.N. Glover, M. Tejeda-Yeomans, *J. High Energy Phys.* **0105**, 010 (2001); Z. Bern, A. De Freitas, L.J. Dixon, *J. High Energy Phys.* **0203**, 018 (2002).
- [24] C. Anastasiou, E.W.N. Glover, C. Oleari, M.E. Tejeda-Yeomans, *Nucl. Phys. B* **605**, 486 (2001); *Phys. Lett. B* **506**, 59 (2001); *J. High Energy Phys.* **0306**, 033 (2003); Z. Bern, A. De Freitas, L.J. Dixon, *J. High Energy Phys.* **0306**, 028 (2003) [*Erratum ibid.* **1404**, 112 (2014)].
- [25] C. Anastasiou, E.W.N. Glover, C. Oleari, M.E. Tejeda-Yeomans, *Nucl. Phys. B* **601**, 318 (2001); **601**, 341 (2001); *Phys. Lett. B* **506**, 59 (2001); A. De Freitas, Z. Bern, *J. High Energy Phys.* **0409**, 039 (2004).
- [26] A. Gehrmann-De Ridder, T. Gehrmann, E.W.N. Glover, *J. High Energy Phys.* **0509**, 056 (2005); J. Currie, E.W.N. Glover, S. Wells, *J. High Energy Phys.* **1304**, 066 (2013); A. Gehrmann-De Ridder, T. Gehrmann, E.W.N. Glover, J. Pires, *Phys. Rev. Lett.* **110**, 162003 (2013); J. Currie, A. Gehrmann-De Ridder, E.W.N. Glover, J. Pires, *J. High Energy Phys.* **1401**, 110 (2014); E.W.N. Glover, J. Pires, *J. High Energy Phys.* **1006**, 096 (2010); A. Gehrmann-De Ridder, E.W.N. Glover, J. Pires, *J. High Energy Phys.* **1202**, 141 (2012); A. Gehrmann-De Ridder, T. Gehrmann, E.W.N. Glover, J. Pires, *J. High Energy Phys.* **1302**, 026 (2013).
- [27] A. Daleo, T. Gehrmann, D. Maitre, *J. High Energy Phys.* **0704**, 016 (2007); A. Daleo, A. Gehrmann-De Ridder, T. Gehrmann, G. Luisoni, *J. High Energy Phys.* **1001**, 118 (2010); R. Boughezal, A. Gehrmann-De Ridder, M. Ritzmann, *J. High Energy Phys.* **1102**, 098 (2011); T. Gehrmann, P.F. Monni, *J. High Energy Phys.* **1112**, 049 (2011); A. Gehrmann-De Ridder, T. Gehrmann, M. Ritzmann, *J. High Energy Phys.* **1210**, 047 (2012).
- [28] J. Currie, T. Gehrmann, J. Niehues, *Phys. Rev. Lett.* **117**, 042001 (2016); J. Currie, T. Gehrmann, A. Huss, J. Niehues, [arXiv:1703.05977](https://arxiv.org/abs/1703.05977) [hep-ph]; X. Chen *et al.*, *J. High Energy Phys.* **1610**, 066 (2016); A. Gehrmann-De Ridder *et al.*, *J. High Energy Phys.* **1611**, 094 (2016); **1607**, 133 (2016).
- [29] S. Dittmaier, A. Huss, C. Speckner, *J. High Energy Phys.* **1211**, 095 (2012).